Analysis of High-Latitude Ionospheric Processes During HSS and CME-Induced Geomagnetic Storms

Durgonics, Tibor; Komjathy, Attila; Verkhoglyadova, Olga; Høeg, Per; Paul, Ashik

Publication date:
2016

Document Version
Publisher's PDF, also known as Version of record

Analysis of High-Latitude Ionospheric Processes During HSS and CME-Induced Geomagnetic Storms

Tibor Durgonics[1], Attila Komjathy[2], Olga P. Verkhoglyadova[2], Per Høeg[1], Ashik Paul[3]

[1]DTU Space, National Space Institute, Department of Geodesy, Copenhagen, Denmark [2]NASA Jet Propulsion laboratory, CA, USA [3]University of Calcutta, Institute of Radio Physics and Electronics, Kolkata, India

Key Points

- Vertical total electron content (VTEC) maps inferred from Greenlandic GNSS stations are used for the first time to investigate differences in ionospheric disturbances caused by high speed streams (HSS) and coronal mass ejections (CME).
- TEC mapping reveals pronounced negative main storm phase and significantly decreased polar patch formation due to increased atmospheric heating.
- On the day following the HSS event (Nov. 4, 2015) a solar radio burst (SRB) caused anomalies in European and Greenlandic air navigation. We present our findings related to this rare event.

Observations and Mapping Technique

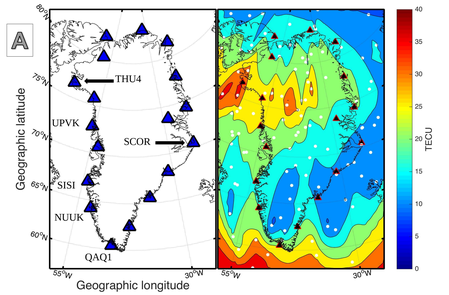

Greenland's GNSS ground stations (a subset of this network can be seen in **Fig A**) present a unique opportunity to observe the high-latitude ionosphere. Due to Greenland's unique location the ground-based GNSS measurements will cover regions representing the polar cap and auroral oval of the ionosphere, providing a complete latitudinal profile of the Arctic ionosphere.

GNSS ionospheric pierce points (IPPs) can be acquired ranging from approxiimately *55* to *90* degrees northern geographic latitudes and *10* to *80* degrees western longitudes.

The geometry behind the calculation of TEC (Hernandez-Pajares et al., 2007) can be seen in **Fig B**. Measurements used in this work consist of *1-second, 15-second, and 30-second* sampling interval using GNSS observations acquired from the Greenland GPS Network (GNET) permanent ground stations located along the Greenland coastline (Durgonics et al, 2017).

From the total number of 62 GNET stations 18 were selected. This selection was based on their geographical location and distance to each other. The goal was to provide an even distribution along the coastline, which resulted in the best IPP coverage. The white dots on the right side panel of **Fig A** shows an example IPP distribution for a given epoch.

The geodetic GNSS receivers are capable of tracking several observables, such as pseudorange observables (*P1* or *C1* and *P2*) and phase observables (*L1, L2*). We utilized the Jet Propulsion Laboratory's Global Ionospheric Maps (JPL GIMs) to obtain VTEC values which then were mapped in 2D, as can be seen in **Fig C**; for details on JPL GIM see, e.g., Mannucci et al. [1998]. **Fig C** shows how the time development of polar patches can be seen on a *non-disturbed* day in the 2D VTEC maps. The time interval between snapshots is *10 minutes*.

Relative plasma drifts are of the order of *1000 m/s* in the polar-cap region, which in theory requires at least *1-Hz* sampling rate to detect *1-km-size* irregularities.

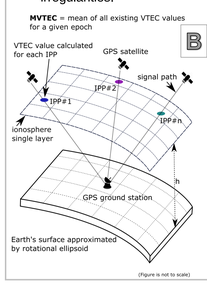

Mean VTEC (MVTEC) (**Fig B**) is calculated as the mean of all the VTEC values obtained from individual data points for a single station. In our approach we used the same weight for each satellite. MVTEC represents a smoothed ionospheric single-layer surface over the given station while its standard deviation indicates how uniformly the ionosphere tends to behave in that region.

$$\frac{dN_e}{dt} = q - \beta N_e - N_e \nabla \boldsymbol{V}^{\perp} - \nabla\left(N_e \boldsymbol{V}^{\parallel}\right) \qquad (1)$$

The F2-layer continuity **Equation (1)** functions as a starting point for the physical interpretation where t is time, q is the production rate, βN_e is the loss rate, $\boldsymbol{V}_{\perp}$ and $\boldsymbol{V}_{\parallel}$ are the perpendicular and parallel components of the bulk plasma velocity, respectively, with respect to the geomagnetic field.

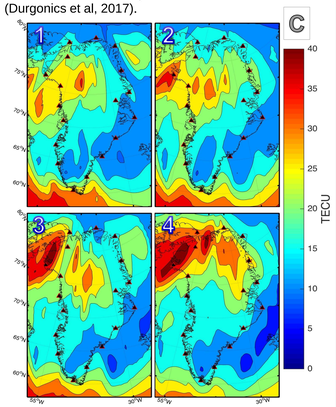

CME-Induced Storm

An example of a larger CME-driven ionospheric storm is the *19 February 2014* highly complex, multiphase storm, which had the largest impact on the disturbance storm-time (Dst) index that year. The geomagnetic storm was the result of two powerful Earth-directed CMEs.

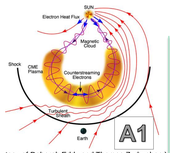

(Courtesy of Deborah Eddy and Thomas Zurbuchen.)

Fig A1 presents a schematic about our current understanding of the complex structure of an interplanetary CME.

HSS-Induced Storm

An example for a larger HSS-driven ionospheric storm is the *3 November 2015* event, which was followed on the next day by a CME and an associated SRB.

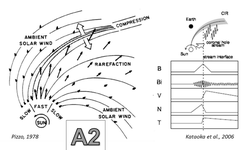

Pizzo, 1978 — Kataoka et al., 2006

Fig A2 shows the interplanetary structure of a HSS and its typical signatures in solar wind parameter data.

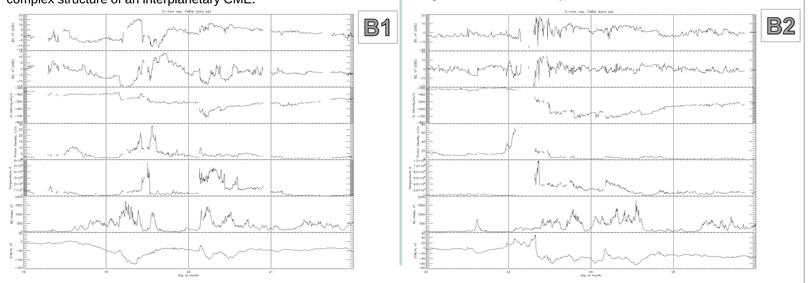

Fig B1 and B2 are relevant (OMNI data) solar wind parameter time-series that demonstrate the differences between the CME and HSS drivers, respectively. One of the important differences can be seen in the behavior of the IMF components. In the HSS case B_z and B_y tend to change sign and fluctuate which will result in sudden electric field changes (Borovsky et al., 2006).

Results

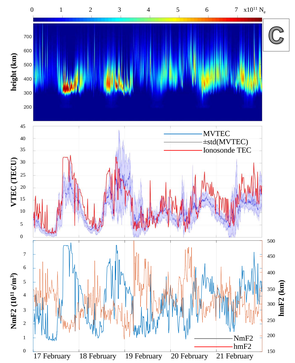

Fig C displays results from Thule during the CME-driven 19 February 2014 storm. Thule is located deep in the polar cap. **Fig C (top):** ionogram-derived profiles showing *5 days* of ionospheric vertical N_e distributions observed by a digital ionosonde. The N_e distributions show that the principle ionized region is the F-layer with hmF2 typically around *300 km*. **FIG C (middle):** MVTEC time series above Thule during the same days as shown in the top image (dark blue line) with the standard deviation of the MVTEC (light blue shading) and the ionosonde-derived TEC (red line). The diurnal ionization cycle in the F-layer was disrupted after the first CME arrival. **Fig C (bottom):** NmF2 and hmF2 time series demonstrating negative correlation.

Fig D: polar cap index (Vennerstrøm et al., 1991) north (PCN) time-series for the CME and HSS-related disturbances. **A** and the red dotted line shows the HSS arrival time and **B** and the blue dashed line marks the CME arrival time. There are fundamental differences between the rate of energy deposition of the two phenomena.

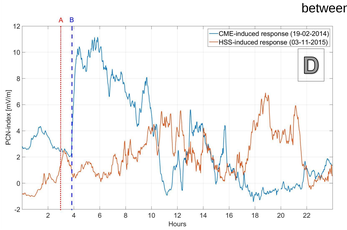

Fig E: MVTEC time-series for the day of the HSS arrival and the following day for a polar cap (**THU4**), an auroral oval (**SCOR**), and a station which is at the equatorward edge of the auroral zone (**QAQ1**).

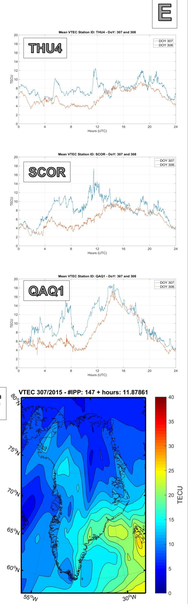

Fig F: VTEC map illustrates the Greenland sector ionosphere during negative ionospheric storm phase (following increasing PCN activity on the day of HSS arrival). A continuous but non-uniform density channel of plasma (tongue of ionization or TOI) is clearly visible.

Solar Radio Burst and Ray Tracing During the Event

Fig A displays a spectrogram observed on ***4 November 2015*** at the Glasgow, Scotland site of the *e-Callisto* solar spectrometer international network. Similar signatures were present at the same times throughout some European sites.

The spectrogram shows the initial detections of a SRB (Knipp et al., 2016), which started at approximately 13:40 UTC and continued for hours. It was observed the day following the *3 November* HSS-related ionospheric disturbances presented in this poster. This SRB disturbed the inflight airport ground radars or the airplane landing receivers in northern Greenland.

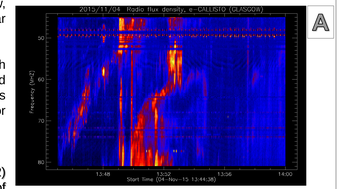

Questions:
(1) Were these disturbances related to the HSS-induced ionospheric storm? (2) At the latitude of Thule, the Sun never rises above the horizon during the days of the storm. Therefore how could air navigation be impacted by solar-originated phenomena?

Facts about the airport:
The direction of the Thule AFB runway with North is: *85 degrees*.
The geographical coordinates of the runway in degrees are: (lat, long) = (*76,53, -68,73*).
The localizer frequency of the inflight radar system is: *109,5 MHz*.

Time of incidence for the received erroneous localizer signal:
Event time: *14:45 UTC (11:45 LT)*

Elevation of the sun:

Local time:	*7:00*	*11:45*	*13:00*
Elevation:	*-15.95*	*-2.87*	*-1.81*
Azimuth:	*89.18*	*157,49*	*175,55*

The sunlit ionosphere for the period November 3-4, 2015:
The F-region (300 km) is sunlit in the period: 7-20 LT (6:30-20:00 LT)
The bottom of the E-region (100 km) is sunlit in the period: 9-18 LT (8:30-18:00 LT)

The E-region (100 km) of the ionosphere is sunlit for angles larger than -10.1 degrees, and the F-region is sunlit for angles larger than -17.3 degrees.

Raytracing of the localizer frequency for plasma frequencies from 10 to 15 MHz:
Radio bursts (less than 190 MHz) will (for elevation angles larger than -3 degrees) be reflected in the E- and F-region of the ionosphere.
Radio bursts (less than 115 MHz) will (for elevation angles between -5 and -3 degrees) be reflected in the E- and F-region of the ionosphere.

Conclusions:
(1) The disturbance was not related to the 3 November HSS event. It was caused by a SRB on the following day.
(2) It is possible to have solar radio bursts (of 109,5 MHz) to impact the ground antenna/cables/wave-guide and the airplane localizer radio.

Summary

For the first time we compared ionospheric effects of HSS and CME-driven storms at high-latitudes. There were similarities and also differences observed in the development of the storms. (1) Both type of storms exhibited clear negative phase, which resulted in an increase of TOI-breaking-down into patches and a decrease in patch formation in general throughout the Greenland sector. The negative phase developed as the PCN-index started to increase indicated energy input into the polar cap. (2) The rate of PCN increase was clearly different for the two types of storms. (3) The impact of the physical processes responsible for the negative phase have less pronounced impact on the diurnal TEC variations than on patch formation.

We also investigated and assessed storm influences on airborne navigation at high-latitudes in order to determine the possible cause of the radio communication disturbances. This effort may lead us to a better understanding of the phenomenon and might help develop communication hardware that is more resistant to such effects.

Bibliography

Borovsky, J. E., and M. H. Denton (2006), Differences between CME-driven storms and CIR-driven storms, J. Geophys. Res., 111, A07S08.
Durgonics, T., A. Komjathy, O. Verkhoglyadova, E. B. Shume, H-H. Benzon, A. J. Mannucci, M. D. Butala, P. Høeg, and R. B. Langley (2017*), Multi-Instrument Observations of a Geomagnetic Storm and its Effects on the Arctic Ionosphere: A Case Study of the 19 February 2014 Storm, Radio Sci. (*under revision).
Hernandez-Pajares, M., J. M. Juan, J. Sanz, and R. Orus (2007), Second-order ionospheric term in GPS: Implementation and impact on geodetic estimates, J. Geophys. Res., 112, B08417.
Kataoka, R., and Y. Miyoshi (2006), Flux enhancement of radiation belt electrons during geomagnetic storms driven by coronal mass ejections and corotating interaction regions, Space Weather, 4, S09004.
Knipp, D. J., et al. (2016), The May 1967 great storm and radio disruption event: Extreme space weather and extraordinary responses, Space Weather, 14, 614–633.
Mannucci, A. J., B. D. Wilson, D. N. Yuan, C. H. Ho, U. J. Lindqwister, and T. F. Runge (1998), A global mapping technique for GPS-derived ionospheric total electron content measurements, Radio Sci., 33(3), 565–582.
Pizzo, V. (1978), A three-dimensional model of corotating streams in the solar wind, 1. Theoretical foundations, J. Geophys. Res., 83(A12), 5563–5572.
Vennerstrøm, S., E. Friis-Christensen, O.A. Troshichev, and V.G. Andrezen (1991) - Comparison between the polar cap index, PC, and the auroral electrojet indices AE, AL, and AU, J. Geophys. Res., 96, 101.

AGU Fall Meeting 2016, San Francisco, USA / 12 – 16 December 2016

SA43C-2399

Contact:
tibdu@space.dtu.dk